ADVANCED MATERIALS INTERFACES Open Access
www.advmatinterfaces.de

A Pathway Toward Sub-10 nm Surface Nanostructures Utilizing Block Copolymer Crystallization Control

Alexander Meinhardt, Peng Qi, Christian David, Ivan Maximov, and Thomas F. Keller**

It is elucidated how crystallization can be used to create lateral surface nanostructures in a size regime toward sub-10 nm using molecular self-assembly of short chain crystallizable block copolymers (BCP) and assist in overcoming the high-χ barrier for microphase separation. In this work, an amphiphilic double-crystalline polyethylene-b-polyethylene oxide (PE-b-PEO) block co-oligomer is used. A crystallization mechanism of the short-chain BCP in combination with neutral wetting of the functionalized substrate surface that permits to form edge-on, extended chain crystal lamellae with enhanced thermodynamic stability. In situ atomic force microscopy (AFM) analysis along with surface energy considerations suggest that upon cooling from the polymer melt, the PE-b-PEO first forms a segregated horizontal lamellar morphology. AFM analysis indicates that the PEO crystallization triggers a morphological transition involving a rotation of the forming extended chain crystals in edge-on orientation. Exposing their crystal side facets to the top surface permits to minimize their interfacial energy and form vertical nanostructures. Moreover, the edge-on lamellae can be macroscopically aligned by directed self-assembly (DSA), one necessity for various nanotechnological applications. It is believed that the observed mechanism to form stable edge-on lamellae can be transferred to other crystallizable short chain BCPs, providing potential pathways for sub-10 nm nanotechnology.

1. Introduction

Molecular self-assembly of block copolymers (BCP) is today used to create structured nanopatterns on thin films exploiting the so called microphase separation arising from the incompatibility between different covalently connected polymer blocks.[1–3] For linear BCPs the resulting morphologies depend on the block incompatibility characterized by the Flory-Huggins interaction parameter χ and the block lengths.[2,4] In thin films, the film thickness in conjunction with the interfacial energy minimization at the free surface and the substrate interface determine the morphology and govern the wetting behavior, nanopattern orientation, and defect density.[1,5–7] For increasingly smaller microphase separated domains constituting of short BCP chains with length N, the driving force for microphase separation ($\chi \times N$) becomes less efficient. To create a sub-10 nm pattern for next-generation lithography therefore requires the use of strongly segregating, so called high χ, low N block copolymers.[1,5,6,8–10]

Arising from the statistical nature of BCP self-assembly perpendicular domains often form in thin BCP films lacking any long-range order, which is undesirable for nanofabrication. In this context, polymer crystallization, which is itself a molecular self-assembly process that creates ordered and selective structures through regular arrangement of polymer chains, can offer attractive means of creating patterned nanostructures with long-range order.[11] Crystallization could provide a complementary, high driving force to assemble nanopattern with ideally increased pattern fidelity. As a nucleation and growth process, the polymer crystal orientation is initially defined by the nuclei, and provided it is not rotating, the forming crystal continues to grow along its growths directions. Existing microphase separated morphologies, interfacial effects, and wetting and dewetting phenomena jointly guide the crystallization with their individual impact.[11]

Indeed, more complex phenomena are involved in crystalline BCP self-assembly compared to amorphous BCPs, and generally, the final morphology depends on the competition between microphase separation and crystallization.[4] The various processes during interactive crystallization can lead to a

A. Meinhardt, T. F. Keller
Centre for X-ray and Nano Science CXNS
Deutsches Elektronen-Synchrotron DESY
22607 Hamburg, Germany
E-mail: alexander.meinhardt@desy.de; thomas.keller@desy.de
A. Meinhardt, T. F. Keller
Department of Physics
University of Hamburg
22607 Hamburg, Germany
P. Qi, C. David
Paul Scherrer Institut
Villigen PSI 5232, Switzerland
I. Maximov
NanoLund and Solid State Physics
Lund University
Lund SE-22100 Lund, Sweden
The ORCID identification number(s) for the author(s) of this article can be found under https://doi.org/10.1002/admi.202400661

DOI: 10.1002/admi.202400661

complex thermodynamic pathway, resulting in different final morphologies.[3,4,8,12–19]

Extended chain crystals represent a subset of polymer crystals in which the chains in the crystal assume a highly stretched conformation (e.g., *all-trans*). Since short-chain oligomers prefer an extended conformation over coil conformation due to the largely reduced conformational entropy and crystallize as extended chain crystals, they are of particular interest for BCP based nanofabrication, offering precise control over pattern size. Furthermore, directed self-assembly (DSA) introduces topographical or chemical patterns that can be utilized, similarly like electrical fields, magnetic fields, or shear forces, to direct the self-assembly of the BCP, align the nanopatterns on a macroscopic scale, and reduce the number of defects.[9,10,20–23]

It is well known that surface-sensitive techniques like atomic force microscopy (AFM) are ideally suited to follow the processes during crystallization in thin films of crystallizable BCPs.[5,11,24–26] The interfacial energy of the BCP with the substrate and atmosphere interface can significantly alter the crystallization kinetics by either hindering or enhancing crystal nucleation and has a strong influence on the polymer crystal orientation and resulting nanopattern, thus offering an additional approach to BCP based nanostructure design.[4,8,13,16,27–32] Therefore, further investigations of crystalline BCP thin film systems are necessary to elucidate the role of crystallization on the nanopattern formation. In this context, a short-chain, double crystalline polyethylene-block-polyethylene oxide (PE-b-PEO) block co-oligomer is an attractive model system which combines amphiphilic properties with biocompatibility, and which forms extended chain crystals, while its homopolymers analogs are widely used.

Moreover, Cao et al. discovered that such a PE-b-PEO in the bulk exhibit more than a single order-to-disorder transition, and passes several stages of morphological transitions upon cooling ranging from a cylindrical phase to gyroid, and finally lamellar morphology at room temperature. They claimed that the morphological transitions were linked to the thermally activated motion of stretched and flexible PE chain segments constrained in geometric confinement rather than being correlated to the PE or PEO crystallization.[33] Sun et al. have found that both PE and PEO blocks of PE-b-PEO co-oligomers in the fully crystalline state form extended chain crystals with PE chains tilted 22° from the lamellar normal and PEO chains parallel to the lamellar normal. In bulk, an interdigitated, single-crystalline layer morphology was observed for both blocks, and the confined PEO crystallization was investigated.[34] Zhang et al. investigated double-crystalline PE-b-PEO BCP bulk-like thick films and found that the topological confinement of the mesophase defined initially by the PE crystallization significantly affected the subsequent PEO crystallization kinetics, although the PEO crystallization then transformed the mesophase into a crystalline lamellar morphology (confined vs breakout crystallization).[15]

While these experiments largely reflect the morphological behavior in the bulk, Schulze et al. observed the formation of vertical lamellae on the top surface of very thin PE-b-PEO films (few L_0 thick, L_0 being the BCP natural pitch) on chemically modified substrates. After drop-casting, the PE-b-PEO initially formed thin films of extended, vertically oriented chains. Depending on the substrate modification, thermal annealing induced a rotation of the extended chains to surface horizontal, leading to the formation of defined, vertical lamellar nanostructures while maintaining the initial film thickness.[3]

Here, we exploit in situ AFM during thermal annealing of a PE-b-PEO thin film to closely monitor the evolution of surface topography during the formation of vertical lamellar nanostructures. Careful tuning of temperature allows to follow film growth, microphase separation, and crystallization under quasi-stationary conditions. We also demonstrate the ability of PE-b-PEO block co-oligomers to form long range ordered surface nanostructures by using topographic guiding patterns for DSA, a prerequisite for potential applications in nanofabrication. Our results highlight the advantage short-chain extended crystal BCPs have over non-crystalline BCPs, which may offer a novel approach for potential application of BCPs in the fabrication of functional nanodevices.

2. Results and Discussion

2.1. Morphology During Thermal Annealing

The PE-b-PEO thin film was prepared by drop casting from ethanol solution on a methyl 3-mercaptopropionate (M3M) functionalized, gold coated Si substrate and thermally annealed for 5 min at 120 °C under constant nitrogen flow on the AFM heating stage and cooled with a rate of 2 °C min^{-1} to 25 °C to create a well-defined, reproducible starting morphology of vertical lamellar nanostructures. Subsequently, the in situ AFM experiments were performed under nitrogen atmosphere.

The film after thermal annealing and during the AFM in situ heating experiments is shown in **Figure 1**. In the AFM phase image of the annealed film shown in Figure 1A we observe vertical nanostructures consisting of vertical lamellae with a 'fingerprint'-like orientation and a lamellar size L_0 of ≈14.6 nm. The general features of the film shown in the large overview AFM height image in Figure 1B always reappear after thermal re-annealing and are divided into several distinct morphologies: islands with vertical lamellae on the outer and sandwich morphologies in the center region, branched dendrites covering the remaining free substrate surface, and large isolated solidified droplets. The distinct morphologies likely form due to variations in polymer concentrations leading to a locally different thickness, and in turn varying conformations and/or crystallization pathways of PE-b-PEO chains on the sample and will be discussed below.

Figure 1C–K shows selected AFM topographic and phase images recorded during the cooling of the PE-b-PEO film from 120 °to 25 °at 10 °C temperature intervals. Starting at 80 °C, the formation of discrete, topographically flat layers was observed. The planar layers continued to grow laterally as temperature was decreased and additional discrete layers appeared on top of the existing layers. The thickness of each discrete layer shown in **Figure 2** (14.5 ± 0.9 nm) is quantized in integers or half-integers of the calculated extended fully crystalline PE-b-PEO chain length d_{ext} = 15.2 nm (calculation shown in the Supporting Information), indicating that the PE-b-PEO chains are oriented vertical with respect to the substrate surface. Further discrete layers grow on top of existing ones as temperature is slowly decreased. The lateral growth progression is apparent from the bright contrast in the AFM phase image in Figure 1F, where one can clearly distinguish between the equilibrated center of the discrete layer and the

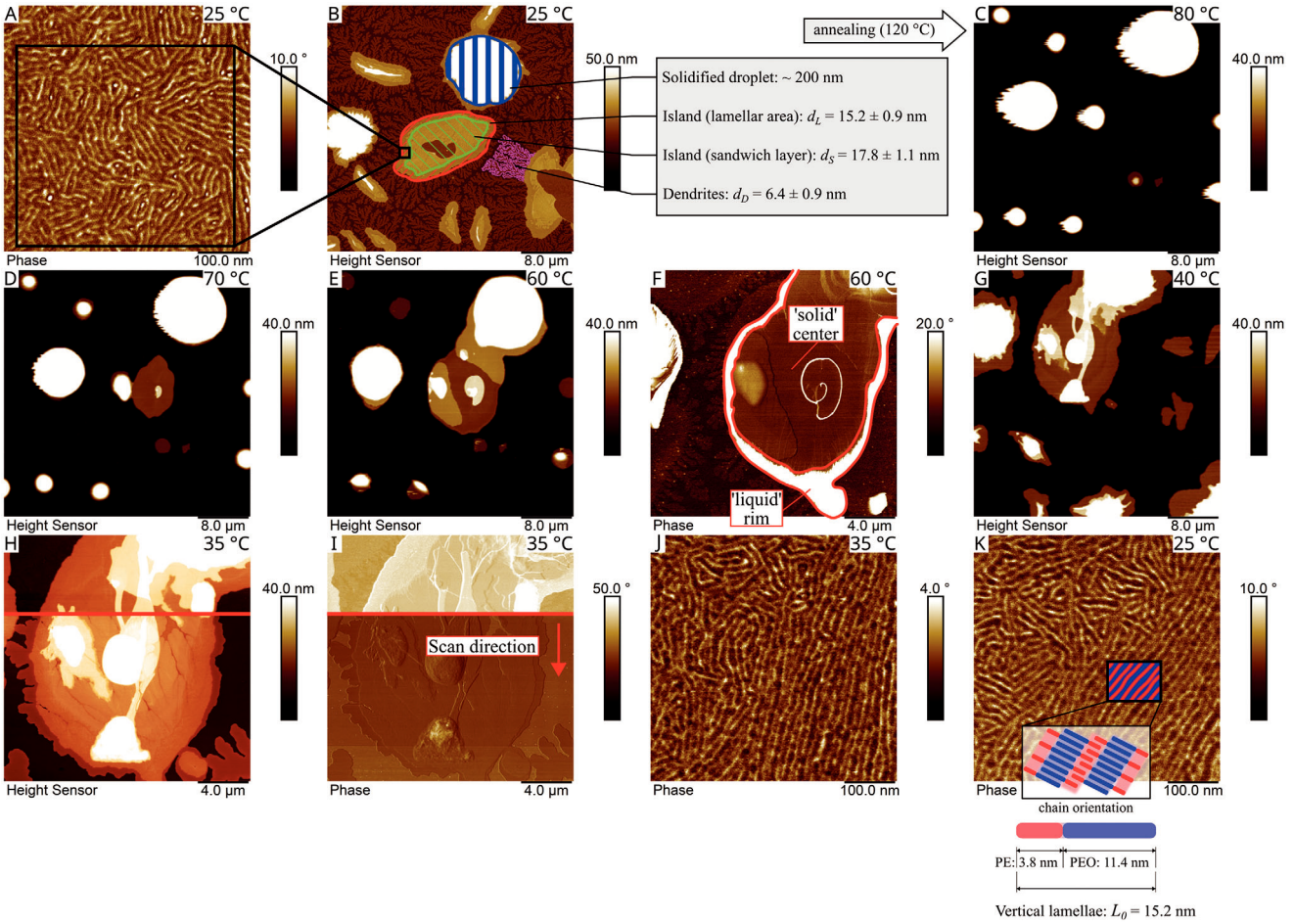

Figure 1. In situ AFM series of the annealed PE-b-PEO thin film. A) High-resolution AFM phase image of the vertical lamellar nanopattern after initial annealing. B) Overview AFM height image showing the sample morphology after initial thermal annealing on the AFM heating stage (heated at 120 °C for 5 min, then cooled with a rate of 2 °C min^{-1} to 25 °C under nitrogen atmosphere). Each distinct feature can be associated with a discrete thickness. The vertical lamellae in (A) are found exclusively on the 15.2 ± 0.9 nm thick area of the island labeled "lamellar area'. Re-annealing at 120 °C leads to dewetting. The temperature was then stepwise reduced while the sample was continuously imaged. Topographically flat layers appeared starting at 80 °C C), and continued to grow laterally as temperature was decreased D-E,G). F) The lateral growth can be visualized in the AFM phase image, with the lateral growth front possessing a 'brighter' contrast. H–J) A fast (1–2 s) sudden transition at 35 °C yields the vertical lamellar nanopattern and various morphologies (dendrites, etc.). K) No reorganization of the lamellae is observed upon reaching 25 °C. The orientation of the PE-b-PEO chains within the lamellae is schematically shown in the inset, together with a sketch of the PE and PEO calculated extended chain block lengths.

"softer" rim of the layer. We assume that lateral growth consumes surrounding BCP chains in the substrate wetting layer and the droplets (see, e.g., Figure S3, Supporting Information). This explains how higher order 'full layers' ($n \bullet d_{ext}$) are often observed on islands near larger droplets.

At 35 °C a sudden transition occurs during the AFM scan. The phase contrast in Figure 1I significantly changes over two scanning lines, corresponding to a timeframe of seconds. While this transition does not change the specific film thicknesses as apparent from Figure 2, new non-integer layers are formed. In the height image in Figure 1H, cracks with 3–4 nm depth appear on the island with the discrete layers, and fingerlike dendrites with a thickness of 7.7 ± 2.7 nm spread from the island outward across the substrate. The high-resolution phase image recorded on an island after the transition (Figure 1J) reveals the formation of vertical lamellae. The mean width L_0 of the lamellae is determined to be 15.9 ± 2.4 nm at 35 °C, which corresponds to the calculated extended chain length d_{ext} within the experimental error, and is also the same as the discrete layer thickness. The formed morphologies remain stable upon reaching room temperature, as seen for the vertical lamellae in Figure 1K, and do not experience any significant change in width (L_0 = 15.9 ± 1.0 nm).

As reported by Schulze et al. the as-cast, unannealed PE-b-PEO film forms discrete terraces of standing extended PE-b-PEO chains.[3] Since it is necessary to delete the thermal history of the sample for our in situ studies, the high chain mobility of the short chain BCP at elevated temperatures results in the formation of the larger droplets observed in Figure 1 and Figure S2 (Supporting Information). However, the dewetting is only partially irreversible. When cooling the system back to room temperature rewetting is observed, with new layers of standing extended chains forming. Compared to Zhang et al.'s cylindrical nanostructures which showed an improved parallel alignment along a growing dewetting front during continuous annealing, our

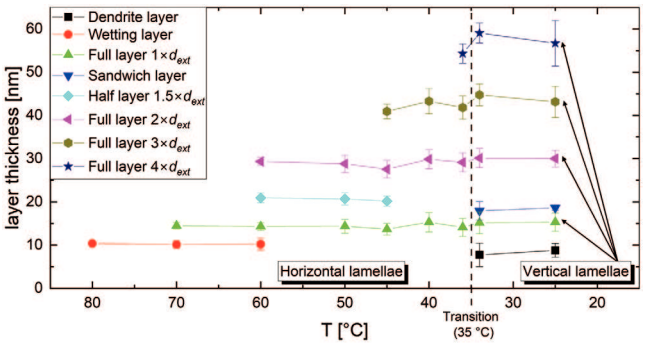

Figure 2. Temperature dependent film thickness of the discrete layers recorded during the in situ AFM series shown in Figure 1. With decreasing temperature, additional layers form on top of existing layers. Most of the layers' thicknesses agree with the calculated extended chain length, indicating standing PE-b-PEO chains (horizontal lamellar morphology). The transition at 35 °C observed in Figure 1 H triggers the reorientation of the horizontal lamellae to vertical lamellae while retaining the original film thickness of the full layers. Note that the vertical lamellae only appear on the full layers with thickness $n \bullet d_{ext}$, with n being a discrete integer number.

PE-b-PEO standing chain layers first grow laterally at a sufficiently low temperature above 35 °C, consuming PE-b-PEO chains from the surrounding droplets and wetting layer.[35] A transition at 35 °C then triggers the vertical lamellae formation on layers with the extended chain thickness. Flow fields at the edge of the layers might locally enhance the lamellar ordering, but the dynamics cannot be resolved with our in situ AFM setup. We speculate that other morphologies (e.g., dendrites) may form depending on the crystallization kinetics, which will be discussed later.

2.2. Influence of Interfacial Energies

The orientation of domains in block copolymer thin films is highly dependent on the interfacial energies between the copolymer blocks and the substrate and the top surface, respectively.[1,5,36–38] The discrete layer thickness L_0 corresponding to d_{ext} measured in Figure 2 indicates that the PE-b-PEO chains at higher temperatures are oriented vertical with respect to the substrate and are fully extended, which is confirmed by the featureless topography of the layers. Therefore, they form a microphase separated horizontal lamellar morphology that is stabilized over the temperature regime from 80 to 35 °C. Contrary, in the bulk, for similar asymmetric BCPs in the same temperature region, various morphologies have been reported.[15,34,39–41] For example, Bates et al. and Weiyu et al. independently observed several phase transitions in asymmetric bulk PE-b-PEO between lamellae, gyroid, cylinder, and spherical structures with temperature.[39,40] As temperature was increased, the lamellae transformed first into a gyroid and cylinder structure, which transformed into a spherical morphology at higher temperatures before disordering. The transitions were closely linked to the melting of the crystalline phases of the PEO and PE blocks.

The key difference from the bulk to the here analyzed, few L_0 thin films is that interfacial effects of the substrate and nitrogen atmosphere interface dominate the microphase evolution.[5] For the few L_0 thin PE-b-PEO BCP films, symmetric, asymmetric, and neutral wetting is distinguished depending on the wetting affinities of both copolymer blocks with the substrate.[3,37] Symmetric and asymmetric wetting both facilitate the formation of a horizontal lamellar morphology, while neutral wetting with a similar interfacial energy difference of both copolymer blocks to the substrate can induce the formation of vertical lamellae.[1,5,36,42] The M3M-functionalized silicon surface has been reported as 'neutral' substrate for PE-b-PEO before, since the water contact angle (76.5 ± 0.9°) lies between that of PE (100–110°) and PEO (0–10°).[3] It is known that the as-cast PE-b-PEO thin film on a M3M surface will assume a discrete thickness corresponding to the standing extended PE-b-PEO chain, where PE or PEO block may be oriented up or down. Lateral segregation of the standing extended PE-b-PEO chains takes place during drop-casting and leads to local domains with the PE and PEO chain end up and down, respectively, and their domain size is limited by the substrate affinity dependent chain mobility. The formation of perpendicular morphologies during thermal annealing ex situ was associated with a thermal barrier for the rotation of the PE-b-PEO chains.[3] Interestingly, we did not observe the formation of a perpendicular morphology in situ upon cooling down from 120 to 35 °C. Instead, the forming PE-b-PEO islands in Figure 1C–G at T = 80 to 35 °C assume a horizontal morphology consisting of standing extended chains, typical for asymmetrical wetting, and the perpendicular morphology only forms at a temperature as low as 35 °C.

In order to explain the asymmetric wetting at elevated temperatures, the interfacial energies between the M3M surface and both copolymer blocks have to be considered. The M3M surface energy can be calculated from contact angle measurements of M3M with, e.g., water and hexadecane using the OWRK method, yielding a surface energy of 34.4 mJ m^{-2}.[43] The details can be inferred from the (Figure S1 and Table S4, Supporting Information). While the M3M substrate surface energy is mostly temperature independent, the PE and PEO blocks both undergo melting and crystallization in the investigated temperature range.[34,39,44] In the melt state, the surface tensions of PE and PEO are mostly dependent on their mass density.[45] By using the Parachor introduced by Sudgen and reported temperature dependent molar volumes of PE and PEO homopolymer analogues (Table S1, Supporting Information), the surface tensions of the PE and PEO blocks in melt state can be estimated.[45–47] As our calculations in the SI show, the surface energies of PE and PEO change significantly upon crystallization ($\Delta\gamma$ between 10–15 mJ m^{-2} for PE and PEO). Note that an extended chain lamellar crystal features two distinct surface facets with different surface energies, which can be extracted from reports of extended chain crystals of PE and PEO homopolymers.[25,48–51] The surface facets consist of the lateral crystal surface γ_L, and the chain-end or ciliated surface γ'. The surface energies and interfacial energies calculated with the Owens-Wendt formula in the Supporting Information are illustrated in **Figure 3**.[1,52]

The interfacial energy of the PEO block at the chain-end surface with the M3M surface at a temperature above the PEO crystallization (T > 35 °C) shown in Figure 3B is clearly lower than the M3M – PE interfacial energy and thus, the PEO favors exposure to the M3M surface. Consequently, the PE block wets the nitrogen interface, as it is the copolymer block with lower

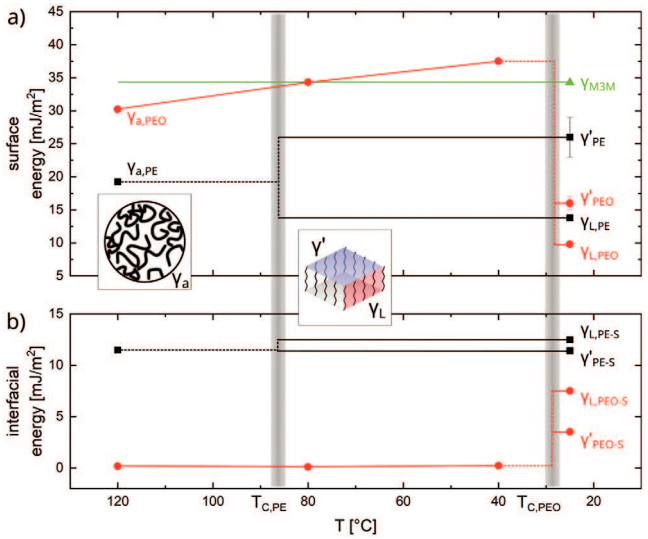

Figure 3. a) Schematic representation of the temperature dependent surface energy evolution of the PE (black), PEO (red), and M3M (green). Upon reaching the PE and PEO crystallization temperatures, the anisotropy of the forming extended chain polymer crystal leads to a distinction between the lower lateral crystal surface energy γ_L and the higher 'cilia'.surface energy γ'. b) Interfacial energy between PE/PEO blocks including their different crystal surfaces and the M3M calculated using the Owens-Wendt formula. A higher interfacial energy indicates a less favorable interaction of the corresponding co-oligomer block with the M3M.

surface energy as seen in Figure 3A, and overall, leads to asymmetric wetting conditions and the horizontal lamellar morphology in the temperature range from 80 to 40 °C. However, this horizontal lamellar morphology is obviously disrupted at 35 °C as evident from the AFM images in Figure 1H,I. At T = 35 °C, PEO starts to crystallize, and simultaneously, vertical lamellae appear, see, e.g., Figure 1J.

2.3. Effect of Thin Film Crystallization

As described earlier and shown in Figure 1I, a morphological transition occurs at 35 °C. The vertical lamellae visible in Figure 1A appear on the outer area of the islands, e.g., in the region marked in red in Figure 1B, and also on all elevated layers which exhibit a thickness corresponding to d_{ext}, indicated as full layers in Figure 2. AFM height images of the vertical lamellae on the elevated layers correspond to Figure 1A and are therefore omitted here. Note that the full layers preserve their film thickness during the transition.

Earlier studies based on ex situ AFM concluded that the lamellae formation mechanism was associated with a thermal barrier for the PE-b-PEO chains and that the standing chains in the as-cast film rotated to form vertical lamellae at elevated temperatures.[3] Since both PE and PEO block may crystallize independently, we can distinguish between three different thermodynamic regimes: the disordered amorphous state (PE amorphous, PEO amorphous), the single-crystalline state (PE crystallized, PEO amorphous), and the double-crystalline state (PE crystallized, PEO crystallized).[34,39] The stark phase contrast change in Figure 1I and the simultaneous appearance of vertical lamellae clearly suggests that the formation of the vertical lamellar nanostructure is directly correlated to the PEO crystallization at 35 °C, rather than a thermally activated chain motion.

Copolymer blocks in BCP thin films can crystallize either flat-on (chains vertical to substrate) or edge-on (chains parallel to substrate), forming crystal lamellae of different orientations.[53] Obviously, the PE-b-PEO chains are oriented vertical in the temperature range from 80 to 40 °C and form a microphase separated lamellar morphology with vertical chains that is driven by the interfacial energy induced preferential exposure of PEO to the M3M surface as outlined above. However, at the transition where PEO starts to crystallize, the chains apparently rotate and form edge-on crystal lamellae by overwriting the microphase separated horizontal morphology despite the existing confinement imposed by the opposite copolymer block, referred to as breakout crystallization.[4,8,19]

The observed breakout crystallization requires that the confinement of the PEO by the crystalline PE block is weak, which seems reasonable to assume, since the PE block (16 ethylene units) is significantly shorter than the PEO block (41 ethylene oxide units). This has been demonstrated for different crystallizable systems, such as PS-b-PLLA, where by switching the crystallization temperature above or below the glass transition of the PS block, the PLLA could either crystallize as edge-on lamellae via breakout crystallization or stay confined in a horizontal geometry.[54]

The PEO crystallization in bulk PE-b-PEO has been reported to change the existing mesostructure from PE single-crystalline lamellae, cylinders, or gyroid to double-crystalline lamellae.[15,34,39,40] Simulations have demonstrated how surface-polymer chain affinity in thin films promotes a surface-assisted nucleation of oriented crystal lamellae.[27,55] While a high affinity between a chain and the surface lead to a reduced chain mobility, a decreased crystallization rate, and in turn, predominantly flat-on crystal lamellae, a low chain affinity with a surface conversely allowed for the formation of predominant edge-on crystals.

The M3M interfacial energy for the PEO block in Figure 3B indeed weakens upon crystallization, which enhances chain mobility and assists in the initial primary PEO nucleation. More importantly, the lateral crystal surface energies of the PE and PEO block, see Figure 3A, possess the lowest surface energy and will be preferably exposed to the nitrogen interface. Since primary PEO nucleation is restricted to the microphase separated horizontal lamellae and may be initiated anywhere in the PEO block, we conclude that the high chain mobility and the surface energy minimization during the proceeding PEO crystallization causes the chains to flip and form vertical lamellae of extended, double-crystalline PE-b-PEO chains. The nucleation may start as flat-on crystallization, but the forming lateral crystal surfaces will reorient the chains and overwrite the horizontal lamellar morphology in order to minimize the free surface energy.

2.4. Crystallization-Dependent Morphologies

The film shown in the overview AFM height image (Figure 1B) can be divided into three distinct morphologies. Besides the vertical lamellae (shown in red) located near the edge of the islands, a slightly thicker top layer, here referred to as "sandwich" layer

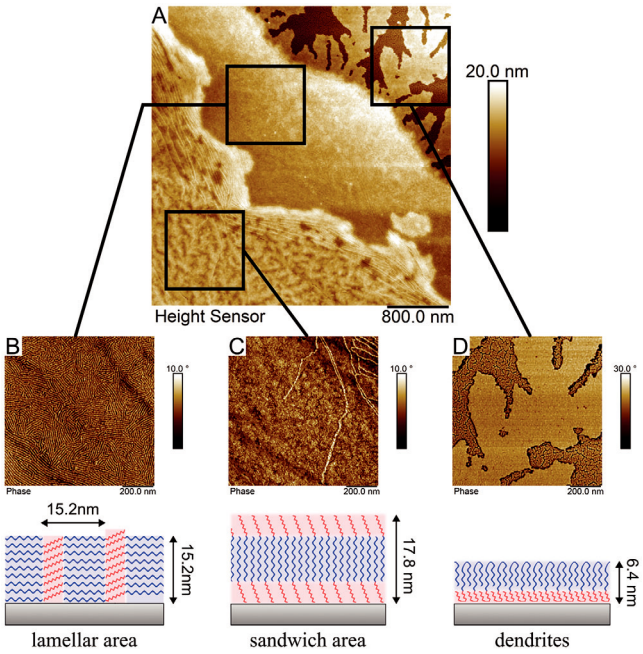

Figure 4. Overview of the final PE-b-PEO thin film morphologies at room temperature after annealing. A) Overview AFM height image and phase images with vertical lamellae region B), sandwich layer region C), and dendrite region D). Each layer has a different thickness stemming from the BCP chain orientation and stacking. The vertical lamellae consist of edge-on, extended chain crystal lamellae (B), while the sandwich (C) and dendrite (D) layers likely consist of flat-on folded-chain crystals.

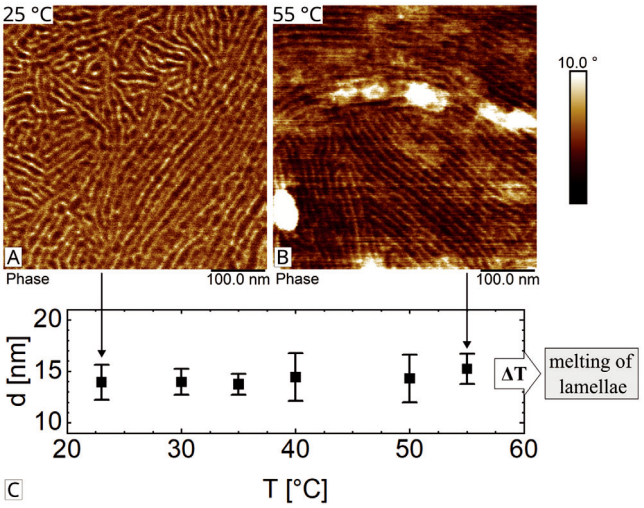

Figure 5. A) AFM phase image of the vertical lamellae at 25 °C and B) at 55 °C. C) Graph of the lamellar width with temperature, demonstrating the thermal stability of the vertical nanopattern up to its melting temperature above 55 °C. Above 55 °C, the lamellar pattern is lost due to melting, thus impeding small-scale, high-resolution AFM imaging.

(shown in green) is in the center of the islands. Finger-like dendrite structures extend from the edge of the islands outward and cover large parts of the bare substrate area (shown in purple). A comparison of the different morphologies, including their location on the thin film, and high-resolution AFM phase images is given in **Figure** 4.

The sandwich layer is featureless and has cracks reaching 3–4 nm down and a thickness of $d_S = 17.8 \pm 1.1$ nm, which is larger than the calculated fully extended chain length ($d_{ext} = 15.2$ nm). The featureless phase image in Figure 4C shows a lack of vertical nanostructures. The additional layer appears first at 35 °C and developed during PEO crystallization. Contrary to the outer region of the island, where the PEO crystallization creates vertical lamellae (Figure 4B) as described in section 2.3, the absence of surface features and the higher thickness indicate that in the central region the PEO crystallization proceeds in a different way. The confinement in the center of the island must be stronger than near the edge of the island and therefore inhibit chain rotation upon PEO crystallization. The sandwich layer probably consists of stacked folded chain crystal morphologies of flat-on oriented crystal lamellae. However, the origin and driving force to create such a chain arrangement is first of all not evident.

For semicrystalline PS-b-PCL and PS-b-PLLA thin films the crystallization was reported to initialize at the edge of islands and the formed crystallites grew inward, producing single edge-on crystals at the edge and on the adsorbed monolayer, which branched and coarsened during crystallization.[8,56] This resulted in the co-existence of multiple morphologies in the thin film.[8] For crystallizable BCPs, the chain stretching due to deformation during hole/island formation will initiate crystallization primarily at the boundaries of the holes or islands.[8]

It is reasonable to assume that the PEO crystallization in the PE-b-PEO thin film is also initiated at the edge of the island due to high chain mobility at the edge and then crystallizes inward.

However, in the center of the island the ability of the chains to rotate upon crystallization is hindered as a consequence of the lateral growth mechanism of the discrete layers above $T_{c,PEO}$ as highlighted in Figure 1F. The difference in phase contrast might indicate different chain mobilities, with BCP chains in the outer area of the island possessing higher mobility, although all chains in the island are confined to the horizontal lamellar morphology before PEO crystallization. Therefore, chain mobility in the horizontal lamellae during PEO crystallization plays a vital role in allowing chain rotation to form vertical lamellae.

The finger-like dendrite structures covering large parts of the bare substrate area in Figure 1B (marked in purple) are topographically featureless and form simultaneously with the sandwich and vertical lamellar morphology at 35 °C as seen in Figure 1H. The PE-b-PEO chains in the dendrites are probably oriented vertically, with the chains forming folded-chain flat-on crystals, since their discrete thickness of 6.4 ± 0.9 nm is smaller than the extended chain length (Figure 4D). They are not perfectly planar, as shown in the (Figure S4, Supporting Information), indicating that the PE-b-PEO chains in the dendrites undergo limited morphological changes during formation similar to relaxations found in thin films of crystalline PEO monolayers, leading to partial chain unfolding.[57] Their lateral structure is typical for surface diffusion-controlled growth, starting from the edges of the islands and growing outward. Chains in the wetting layer on the M3M surface will diffuse toward the forming growth front, where they will attach themselves to the crystal, thus changing their planar

arrangement toward a more vertical arrangement.[25,57] The depletion of chains in the wetting layer will then lead to the finger-like growth.

For low molecular weight PEO fractions with lengths as short as ≈6 nm, once-folded chain crystals were reported to crystallize at high undercoolings by Godovsky et al., while at small undercoolings the short-chain PEO oligomers preferably formed extended chain crystals.[50]

Although short-chain block co-oligomers prefer an extended conformation, they may form a folded-chain crystal instead of an extended chain crystal at sufficiently high undercoolings. High undercooling can also be understood as fast crystallization, limiting chain reorganization, or in this case, chain unfolding. As observed by the fast topographical transition in Figure 1H over 1–2 lines (corresponding to a timeframe of 1–2 s), the PEO crystallization proceeds very quickly, therefore promoting the formation of dendrites on the bare substrate area as folded-chain flat-on crystals.

Summarizing, our results suggests that the PE-b-PEO chains in both sandwich and dendrite morphology are vertically oriented with respect to the M3M surface and consist of folded chain crystals. They and the vertical lamellae form simultaneously upon PEO crystallization via different crystallization pathways, depending on the mobility of the chains and their orientation in the wetting layer or in the single-crystalline horizontal lamellae.

Since short-chain co-oligomers favor an extended conformation, we hypothesize that the extended chain lamellae are more stable than the arrangement in the sandwich and dendrite layers. We therefore investigated the melting of the vertical lamellae and the melting of the sandwich and dendrite morphologies, see, e.g., **Figures 5** and S2 (Supporting Information), respectively. As the temperature increased, the dendrite and sandwich structures began to exhibit some lateral segregation at 45 °C, as illustrated in the AFM height image in Figure S2E (Supporting Information). Further increase of the temperature to 50 °C as shown in Figure S2F (Supporting Information) lead to complete melting of the dendrites, and the sandwich layer thickness decreased to the extended chain length and formed a topographically flat surface in the center of the island. On the other hand, the vertical lamellae in Figure 5 remained stable and disappeared only above 55 °C, the melting temperature of the PEO block.[3] This proves that the folded-chain sandwich and dendrite morphologies are as expected less thermally stable than the fully extended chain crystals of the vertical lamellae.

Folded-chain crystals are known to be less thermodynamically favored than their extended chain counterpart. Reiter et al. used kinetic control of the PEO crystallization in a PB-b-PEO BCP to study the folding and unfolding of chains at different crystallization temperatures.[11] The folded-chain crystal lamellae formed under kinetic control at high undercoolings transformed into their thermodynamic stable extended-chain lamellar state by thermal annealing below $T_{m,PEO}$. With this transition, the orientation of the lamellae changed from vertical to horizontal. Compared to kinetically crystallized vertical nanostructures our results highlight the thermodynamic stability of vertical lamellae of extended, short-chain PE-b-PEO crystals and clearly demonstrates the advantageous stability and homogenous feature size this BCP systems has over other crystallizable BCP.

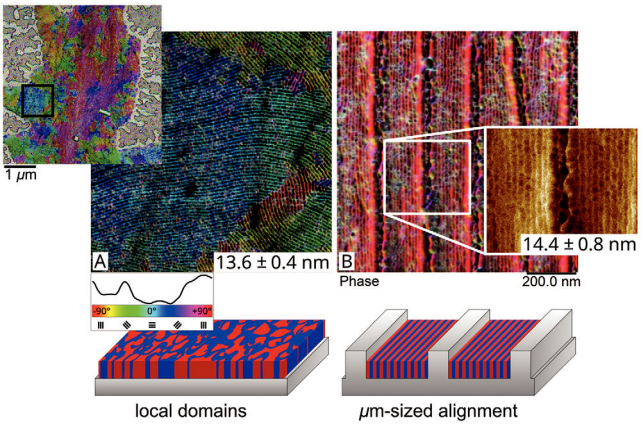

Figure 6. AFM phase images of lamellar nanostructures of PE-b-PEO on planar (no DSA) and structured (with DSA) substrates. A) Vertical nanopattern on planar substrate, showing local alignment. The color scale refers to the orientation of the domains (a schematic graph of the orientation distribution is shown above the color scale, showing preferential alignment for specific directions on the island), the top left shows a 5 × 5 μm overview. B) Aligned BCP along DSA trench pattern (150 nm trench width) with inset, demonstrating the macroscopic, long-range alignment, here over several μm. The images clearly show how the alignment is improved over the whole image compared to the case without DSA. The DSA has no influence on the width L_0 of the vertical lamellae.

2.5. Directed Self-Assembly

The macroscopic alignment of the lamellar nanopattern using trench pattern was investigated. **Figure 6B** depicts the PE-b-PEO lamellae aligned along the trench direction of a 150 nm wide and 50 nm deep periodic trench pattern. The polymer processing to create the nanostructured thin PE-b-PEO film was kept the same as for the plane, chemically modified Si surfaces. In order to compare the effect of the DSA on the nanolamellae orientation, Figure 6A depicts AFM phase images of PE-b-PEO lamellae recorded on unstructured planar substrates. The colormap in Figure 6 indicates the orientation of the lamellae which was determined with OrientationJ, a plugin for ImageJ image processing software.[58] The lamellar thickness L_0 remained the same independent of the DSA.

BCP thin film self-assembly on a planar substrate inevitably leads to the formation of local domains of different lateral-oriented nanopatterns with numerous defect structures, thus limiting their use in applications.[20] In order to be used in nanotechnology, the BCP nanopattern self-assembly must be guided into the desired long-range order, orientation, and morphology.[21] Different approaches for DSA include utilizing external fields (shear, electrical), chemically patterned substrates (chemoepitaxy), or topographic guiding patterns (graphoepitaxy).[20,21,30,59–61]

Here we show that our double-crystalline PE-b-PEO BCP can be macroscopically aligned as a first required step toward nanofabrication. Our electron beam lithography-fabricated (EBL), hydrogen silsesquioxane-based (HSQ) trench patterns were uniformly functionalized with M3M, providing neutral wetting affinity for the BCP at the bottom and sides of the trenches. As shown in Figure 6B, the vertical lamellae align along the

direction of the trench length, forming an ordered array of vertical nanostructures over a range of several µm. In comparison, the vertical lamellae on the unstructured substrate in Figure 6A show local alignment of varying degree in small domains. Several bridge-like features observed in Figure 6 are likely the result of singular defects and branching of the vertical lamellae. They may be caused by incomplete breakout crystallization during formation of the vertical lamellae, indicating lower local crystallinity. We speculate that the defect density could be reduced by decreasing the trench height of the guiding lines. Likely, the bridge-like features are also partially induced by AFM tip-related issues from the challenging imaging inside the trenches.

Although improved local domain order with lamellae highly oriented along the direction of the edge of the film could be observed, the vertical lamellae on the unstructured substrate have a heterogeneous morphology, making them undesirable for nanofabrication. The local alignment on the unstructured substrate stems from a dewetting process at the three-phase contact line between air, substrate, and BCP film.[11] A flow field provided by diffusion of the BCP chains can locally order the BCP nanostructures.[35] However, BCP-based applications require macroscopic alignment of the vertical lamellae and direct control over their orientation.

To our knowledge, this is the first report that demonstrates the macroscopic alignment of a double-crystalline PE-b-PEO BCP with graphoepitaxy based DSA. Further studies are necessary to elucidate how the PE-b-PEO pattern of macroscopically aligned vertical lamellae can be subsequently processed.

Typical processing steps include the selective (metal)-ion infiltration of a copolymer block (e.g., sequential infiltration synthesis), followed by a pattern transfer step through etching.[62,63] Ghoshal et al. have demonstrated the processability of a polystyrene-b-polyethylene oxide BCP. By selective metal ion infiltration of the PEO block and subsequent processing, large scale silicon and iron oxide nanowire arrays were produced by an etch step, utilizing the infiltrated BCP as a mask.[2,63,64] In principle, this methodology could be employed using PE-b-PEO as an promising BCP candidate for nanofabrication.

3. Conclusion

We have investigated the formation of vertical surface nanostructures and the role of crystallization in thin films of a short chain, double-crystalline PE-b-PEO block copolymer. At elevated temperatures, the PE-b-PEO forms thin films of horizontal lamellae with PE at the nitrogen interface and PEO wetting the M3M substrate interface due to interfacial effects. Upon PEO crystallization, the BCP transforms from horizontal to vertical lamellae by chain rotation. The chain rotation is the result of surface energy minimization promoting the exposure of the lateral crystal surface to the nitrogen interface, leading to edge-on growth of crystal lamellae. The vertical lamellae were shown to be thermodynamically more stable compared to other morphologies found in the film. The other morphologies formed in regions with lower chain mobility, which mainly lead to flat-on crystallization of folded chains. The thermodynamic stability of the vertical nanopattern due to the extended chain conformation, together with the exact lamellar thickness corresponding to the extended chain length, offers a clear advantage over vertical nanopattern produced via non-crystalline BCPs or via kinetically controlled crystallization (with, e.g., folded chain crystals).

Additionally, the domain structures of the vertical nanopattern were shown to locally align along the dewetting borders of the film, likely due to internal stress fields and preferential nucleation at the three-phase-contact line. Trench guiding patterns could align the lamellar domains macroscopically, demonstrating the feasibility of short-chain PE-b-PEO based surface structures and providing a first step toward future fabrication of functional nanodevices.

4. Experimental Section

Materials: Polyethylene-block-poly(ethylene oxide) with a nominal average molar mass of 2250 g mol^{-1} and 80 wt.% PEO was purchased from VWR International. Methyl 3-mercaptopropionate (M3M, 98% purity) was purchased from Thermo Fischer Scientific. Ethanol (absolute) was purchased from Sigma-Aldrich and acetone was purchased from VWR International. The block lengths and theoretical extended total chain length were calculated using the molar mass and PEO weight percentage as shown in the Supporting Information. Estimation of the Flory–Huggins interaction parameter χ via Hildebrand solubility parameters δ_H is also shown in the Supporting Information.

Substrate Preparation: A silicon wafer was cut in 1 × 1 cm^2 pieces and sonicated in acetone, ethanol, and ultrapure water, then dried with compressed nitrogen. A 5 nm gold film was deposited on the substrate via sputter coating. The substrate was then rinsed with ethanol, dried with compressed nitrogen, and subsequently cleaned in argon plasma for 5 min. For surface modification with self-assembled monolayers, the substrate was immersed in a 5 mM solution of methyl 3-mercaptopropionate in ethanol for 2 h and afterward rinsed with ethanol, dried with compressed nitrogen, and stored in vacuum at 80 °C for 1 h. The same surface modification was also applied to the guiding patterns fabricated by electron beam lithography for directed self-assembly described below.

DSA Pattern Fabrication via Electron Beam Lithography (EBL): Trench patterns suitable for guiding the self-assembly of the PE-b-PEO were fabricated via EBL at Paul Scherrer Institute (PSI), Switzerland. A silicon chip (1 × 1 cm^2) was cleaned in O_2 plasma for 60 s. After pre-baking at 125 °C, the chip was spin-coated with hydrogen silsesquioxane (HSQ) resist (2% XR1541, Dow Corning) at 3000 rpm with 1000 rpm s^{-1} acceleration for 60 s. EBL was performed with a Vistec EBPG 5000+ using a 100 kV electron beam, 1 nA beam current, and 300 µm aperture. The exposure dose was varied from 9000 to 14500 µC cm^{-2}. After exposure, the patterns were developed in a 1:3 solution of Microposit 351 and water for 60 s. The pattern was then sputter coated with 10 nm Au. The total height of the trench pattern was ≈50–70 nm, with a line thickness of ≈30–50 nm, and varying trench sizes (50, 100, 150 nm). The trench patterns were written in separated 100 × 100 µm sized squares for each dose and trench size.

Thin Film Preparation: Thin films of PE-b-PEO block copolymer were prepared by drop casting a 0.1 wt.% PE-b-PEO solution in ethanol on the M3M modified substrates. To induce the formation of perpendicular nanostructures, the BCP films were thermally annealed with the heating stage of the AFM in dry nitrogen atmosphere by heating at 120 °C for 5 min and subsequently cooling to room temperature at a constant rate of 2 °C min^{-1}.

In situ AFM Investigation: The annealed films were investigated with a Dimension Icon AFM (Bruker) with an integrated heating stage.[65] For the in situ measurements, RTESP-150 cantilever (Bruker) without a reflective coating was used to avoid bimetallic bending effects during heating, and the cantilever was kept at the same temperature as the sample on the heating stage. The sample was placed on a heating stage and was continuously imaged while the temperature was slowly changed. When necessary, the cantilever tip was withdrawn and the laser was realigned due to the heat induced bending. The sample was imaged under constant N_2 flow

(30 ccm min^{-1}). The tip heater was switched in automatic mode. For the in situ study, the film was slowly heated in 5 °C steps until 120 °C was reached, and the AFM image was recorded every 10 °C steps after the image stabilized. The same procedure was applied when cooling the sample down to room temperature. For high resolution scan sizes (< 5 × 5 µm) at elevated temperature, the AFM tip induced the formation of larger agglomerates on the BCP film.

For the analysis of the layer thickness, the AFM height images were processed by masking the island regions and subsequent plane fitting or flattening of the blank substrate area. The thickness of each layer was determined by the height distribution in the height images and confirmed with individual line profiles.

Supporting Information

Supporting Information is available from the Wiley Online Library or from the author.

Acknowledgements

The authors thank Arti Dangwal Pandey and Bojan Bosnjak, DESY, for supporting the EBL preparation of the DSA templates and Arno Jeromin, DESY, for support in microscopy. The work has received support from the EU H2020 framework program for research and innovation under grant no. 101007417 Nano-science Foundries and Fine Analysis (NFFA-Europe-Pilot). A. Meinhardt, T. F. Keller acknowledge support by the Helmholtz Foundation through the Helmholtz-Lund International Graduate School (HELIOS, HIRS-0018). I. Maximov acknowledges financial support by NanoLund.

Open access funding enabled and organized by Projekt DEAL.

Conflict of Interest

The authors declare no conflict of interest.

Data Availability Statement

The data that support the findings of this study are openly available in [Zenodo] at [https://doi.org/10.5281/zenodo.14202741], reference number [14202741].

Keywords

crystallization, diblock copolymer, directed self-assembly, extended chain, in situ AFM, vertical nanostructure

Received: August 9, 2024
Revised: January 27, 2025
Published online: February 10, 2025

[1] K. Brassat, J. K. N. Lindner, *Adv. Mater. Interfaces.* **2020**, *7*, 1901565.
[2] C. Sinturel, F. S. Bates, M. A. Hillmyer, *ACS Macro Lett.* **2015**, *4*, 1044.
[3] R. Schulze, M. M. L. Arras, G. Li Destri, M. Gottschaldt, J. Bossert, U. S. Schubert, G. Marletta, K. D. Jandt, T. F. Keller, *Macromolecules* **2012**, *45*, 4740.
[4] C. De Rosa, R. Di Girolamo, A. Malafronte, M. Scoti, G. Talarico, F. Auriemma, O. Ruiz de Ballesteros, *Polymer* **2020**, *196*, 122423.
[5] M. J. Fasolka, A. M. Mayes, *Annu. Rev. Mater. Res.* **2001**, *31*, 323.
[6] C. M. Bates, M. J. Maher, D. W. Janes, C. J. Ellison, C. G. Willson, *Macromolecules* **2014**, *47*, 2.
[7] J. N. Murphy, K. D. Harris, J. M. Buriak, *PLoS One* **2015**, *10*, e0133088.
[8] W. N. He, J. T. Xu, *Prog. Polym. Sci.* **2012**, *37*, 1350.
[9] R. Ma, X. Zhang, D. Sutherland, V. Bochenkov, S. Deng, *Int. J. Extrem. Manuf.* **2024**, *6*, 062004.
[10] Y. H. Chung, J. K. Oh, *Biosensors* **2024**, *14*, 542.
[11] G. Reiter, G. Castelein, P. Hoerner, G. Riess, A. Blumen, J. U. Sommer, *Phys. Rev. Lett.* **1999**, *83*, 3844.
[12] E. Matxinandiarena, A. Múgica, M. Zubitur, V. Ladelta, G. Zapsas, D. Cavallo, N. Hadjichristidis, A. J. Müller, *Polymers* **2021**, *13*, 3133.
[13] O. Dolynchuk, T. Thurn-Albrecht, *Macromol. Chem. Phys.* **2023**, *224*, 2200455.
[14] A. Cicolella, F. De Stefano, M. Scoti, G. Talarico, J. M. Eagan, G. W. Coates, R. Di Girolamo, C. De Rosa, *Macromolecules* **2024**, *57*, 2230.
[15] X. Zhang, R. Schulze, P. Zhang, C. Lüdecke, X. Zhang, Z. Su, K. D. Jandt, *Polymer* **2014**, *55*, 1893.
[16] S. Nakagawa, H. Marubayashi, S. Nojima, *Eur. Polym. J.* **2015**, *70*, 262.
[17] L. Sangroniz, B. Wang, Y. Su, G. Liu, D. Cavallo, D. Wang, A. J. Müller, *Prog. Polym. Sci.* **2021**, *115*, 101376.
[18] R. M. Michell, A. J. Müller, *Prog. Polym. Sci.* **2016**, *54–55*, 183.
[19] W. Xu, Y. Zheng, P. Pan, *J. Polym. Sci.* **2022**, *60*, 2136.
[20] M. Luo, T. H. Epps, *Macromolecules* **2013**, *46*, 7567.
[21] C. Pinto-Gómez, F. Pérez-Murano, J. Bausells, L. G. Villanueva, M. Fernández-Regúlez, *Polymers* **2020**, *12*, 2432.
[22] S. B. Darling, *Prog. Polym. Sci.* **2007**, *32*, 1152.
[23] D. Lu, V. A. Bobrin, *Biomacromolecules* **2024**, *25*, 7058.
[24] C. M. Papadakis, C. Darko, Z. Di, K. Troll, E. Metwalli, A. Timmann, G. Reiter, S. Förster, *Eur. Phys. J. E.* **2011**, *34*, 7.
[25] G. Reiter, G. Castelein, P. Hoerner, G. Riess, J. U. Sommer, G. Floudas, *Eur. Phys. J. E.* **2000**, *2*, 319.
[26] G. Reiter, G. Castelein, J. U. Sommer, *Macromol. Symp.* **2002**, *183*, 173.
[27] Y. Ming, T. Hao, Z. Zhou, S. Zhang, Y. Nie, *Cryst. Growth Des.* **2023**, *23*, 7653.
[28] D. Lin, H. Wei, J. Wei, J. Xu, C. Zhang, X. Wang, *Macromolecules* **2024**, *57*, 2801.
[29] R. V. Castillo, A. J. Müller, *Prog. Polym. Sci.* **2009**, *34*, 516.
[30] C. De Rosa, R. Di Girolamo, A. Cicolella, G. Talarico, M. Scoti, *Polymers* **2021**, *13*, 2589.
[31] H. Schmalz, V. Abetz, *Polymers.* **2022**, *14*, 696.
[32] L. Chu, W. J. B. Grouve, M. van Drongelen, E. G. de Vries, R. Akkerman, M. B. de Rooij, *Adv. Mater. Interfaces.* **2021**, *8*, 2001894.
[33] W. Cao, K. Tashiro, H. Masunaga, S. Sasaki, M. Takata, *J. Phys. Chem. B* **2009**, *113*, 8495.
[34] L. Sun, Y. Liu, L. Zhu, B. S. Hsiao, C. A. Avila-Orta, *Polymer* **2004**, *45*, 8181.
[35] H. Zhang, B. Wang, G. Wang, C. Shen, J. Chen, G. Reiter, B. Zhang, *Macromolecules* **2020**, *53*, 9631.
[36] L. Li, X. Jia, Q. Dong, J. Zhou, W. Li, *Macromolecules* **2023**, *56*, 5932.
[37] M. J. Fasolka, P. Banerjee, A. M. Mayes, G. Pickett, A. C. Balazs, *Macromolecules* **2000**, *33*, 5702.
[38] X. Chevalier, G. Pound-Lana, C. G. Correia, S. Cavalaglio, B. Cabannes-Boué, F. Restagno, G. Miquelard-Garnier, S. Roland, C. Navarro, G. Fleury, M. Zelsmann, *Nanotechnology* **2023**, *34*, 175602.
[39] M. A. Hillmyer, F. S. Bates, *Macromol. Symp.* **1997**, *117*, 121.
[40] C. Weiyu, K. Tashiro, M. Hanesaka, S. Takeda, H. Masunaga, S. Sasaki, M. Takata, *J. Phys. Conf. Ser.* **2009**, *184*, 012003.
[41] R. V. Castillo, M. L. Arnal, A. J. Müller, I. W. Hamley, V. Castelletto, H. Schmalz, V. Abetz, *Macromolecules* **2008**, *41*, 879.
[42] J. N. L. Albert, T. H. Epps, *Mater. Today* **2010**, *13*, 24.
[43] C. D. Bain, E. B. Troughton, Y. T. Tao, J. Evall, G. M. Whitesides, R. G. Nuzzo, *J. Am. Chem. Soc.* **1989**, *111*, 321.

[44] J. P. Yang, Q. Liao, J. J. Zhou, X. Jiang, X. H. Wang, Y. Zhang, S. D. Jiang, S. K. Yan, L. Li, *Macromolecules* **2011**, *44*, 3511.
[45] D. W. Van Krevelen, K. Te Nijenhuis, *Properties of Polymers*, 4th ed., Elsevier, Amsterdam **2009**.
[46] S. Sugden, *J. Chem. Soc., Trans.* **1924**, *125*, 1177.
[47] G. T. Dee, T. Ougizawa, D. J. Walsh, *Polymer.* **1992**, *33*, 3462.
[48] J. D. Hoffman, *Polymer* **1991**, *32*, 2828.
[49] J. D. Hoffman, R. L. Miller, *Polymer* **1997**, *38*, 3151.
[50] Y. K. Godovsky, G. L. Slonimsky, N. M. Garbar, *J. Polym. Sci. Part C Polym. Symp.* **1972**, *38*, 1.
[51] P. C. Hiemenz, T. P. Lodge, *Polymer Chemistry*, 2nd ed., CRC Press, Boca Raton, FL **2007**.
[52] D. K. Owens, R. C. Wendt, *J. Appl. Polym. Sci.* **1969**, *13*, 1741.
[53] W. Hu, D. Frenkel, *Faraday Discuss.* **2005**, *128*, 253.
[54] J. Fu, Y. Wei, L. Xue, B. Luan, C. Pan, B. Li, Y. Han, *Polymer.* **2009**, *50*, 1588.
[55] Y. Ma, W. Hu, G. Reiter, *Macromolecules* **2006**, *39*, 5159.
[56] F. Zhang, Y. Chen, H. Huang, Z. Hu, T. He, *Langmuir* **2003**, *19*, 5563.
[57] G. Reiter, J. U. Sommer, *J. Chem. Phys.* **2000**, *112*, 4376.
[58] Z. Püspöki, M. Storath, D. Sage, M. Unser, In *Focus Bio-Image Informatics*, (Eds.: W. H. De Vos, S. Munck, J.-P. Timmermans), Springer International Publishing, Cham **2016**, pp. 69.
[59] P. W. Majewski, K. G. Yager, *J. Phys. Condens. Matter* **2016**, *28*, 403002.
[60] J. Zhang, X. Yu, P. Yang, J. Peng, C. Luo, W. Huang, Y. Han, *Macromol. Rapid Commun.* **2010**, *31*, 591.
[61] C. Park, J. Yoon, E. L. Thomas, *Polymer* **2003**, *44*, 6725.
[62] L. Wilson, International Technology Roadmap for Semiconductors (ITRS), *Semiconductor Industry Association* **2013**, 1.
[63] A. Löfstrand, A. Vorobiev, M. Mumtaz, R. Borsali, I. Maximov, *Polymers* **2022**, *14*, 654.
[64] T. Ghoshal, C. Ntaras, J. O'Connell, M. T. Shaw, J. D. Holmes, A. Avgeropoulos, M. A. Morris, *Nanoscale* **2016**, *8*, 2177.
[65] A. Stierle, T. F. Keller, H. Noei, V. Vonk, R. Roehlsberger, *J. large-scale Res. Facil. JLSRF* **2016**, *2*, A76.